LANGMUIR

pubs.acs.org/Langmuir Article

Nanoconfinement of Carbon Dioxide within Interfacial Aqueous/Ionic Liquid Systems

Published as part of Langmuir virtual special issue "Highlights in Interface Science and Engineering: Reactive Separations for Carbon Capture".

Calen J. Leverant, Danielle Richards, Erik D. Spoerke, Ryan Alcala, Ying-Bing Jiang, Stephen J. Percival, Juan M. Vanegas,* and Susan B. Rempe*

Cite This: *Langmuir* 2024, 40, 10615−10622 Read Online

ABSTRACT: Nanoporous, gas-selective membranes have shown encouraging results for the removal of CO_2 from flue gas, yet the optimal design for such membranes is often unknown. Therefore, we used molecular dynamics simulations to elucidate the behavior of CO_2 within aqueous and ionic liquid (IL) systems ([EMIM][TFSI] and [OMIM]-[TFSI]), both confined individually and as an interfacial aqueous/IL system. We found that within aqueous systems the mobility of CO_2 is reduced due to interactions between the CO_2 oxygens and hydroxyl groups on the pore surface. Within the IL systems, we found that confinement has a greater effect on the [EMIM][TFSI] system as opposed to the [OMIM][TFSI] system. Paradoxically, the larger and more asymmetrical $[OMIM]^+$ molecule undergoes less efficient packing, resulting in fewer confinement effects. Free energy surfaces of the nanoconfined aqueous/IL interface demonstrate that CO_2 will transfer spontaneously from the aqueous to the IL phase.

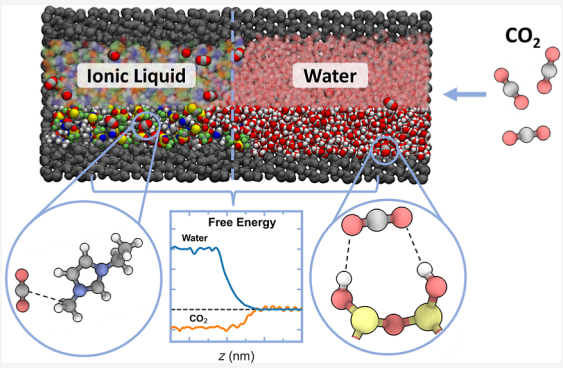

INTRODUCTION

Ionic liquids (ILs) have garnered much attention for their unique and advantageous properties.[1,2] Notably, ILs have negligible volatility, high chemical stability, and a large range of useful operating temperatures.[3−5] These properties, as well as the fact that many ILs possess high carbon dioxide (CO_2) solubility, make ILs promising candidates to replace aqueous amines in postcombustion capture of CO_2.[6,7] For this reason, extensive research has been dedicated to understanding and enhancing CO_2 solubility and transport in ILs.[8−13] One drawback of ILs is that their high cost relative to traditional solvents has led some techno-economic analyses to suggest that it might not be viable to use large quantities of physically absorbing IL for CO_2 capture.[14,15] However, this drawback can be remedied by the development of novel systems that use considerably less of the expensive IL component, such as thin film[16] and membrane systems.[17]

Initial work integrating ILs into gas-selective polymer membranes by Noble[18,19] and others[20,21] achieved excellent performance, with CO_2/N_2 selectivity as high as 61.[22] Maginn's group performed molecular simulations of graphite slit pore IL membranes, finding that nanoconfinement may increase the permselectivity for CO_2 over CH_4.[23] Yet, further optimization is difficult as a trade-off between selectivity and permeability typically exists.[24] Fu et al. achieved unprecedently high performance, including a CO_2/N_2 selectivity of 788 and a CO_2 flux of 2600 GPU, using ultrathin water (H_2O) membranes to stabilize the enzyme carbonic anhydrase (CA) at concentrations greater than those attainable in bulk water.[25] The gas separation membrane proposed by Fu et al. could be redesigned to include an IL layer directly following the ultrathin CA-catalyzed aqueous layer. This new system would enable the CO_2 transported through the membrane to be concentrated into a condensed phase for easier conversion into value-added products.

Previously, we used both classical molecular dynamics (MD) and laboratory experiments to investigate the behavior of CO_2 in bulk, interfacial aqueous-[EMIM][TFSI] and aqueous-[OMIM][TFSI] systems,[26] where $[EMIM]^+$ = 1-ethyl-3-methylimidazolium, $[OMIM]^+$ = 1-octyl-3-methylimidazolium, and $[TFSI]^-$ = bis(trifluoromethanesulfonyl)imide (Figure 1a). We observed that CO_2 will transport spontaneously from the aqueous phase to the IL phase and that the diffusion of

Received: February 14, 2024
Revised: April 17, 2024
Accepted: April 19, 2024
Published: May 8, 2024

https://doi.org/10.1021/acs.langmuir.4c00542
Langmuir 2024, 40, 10615−10622

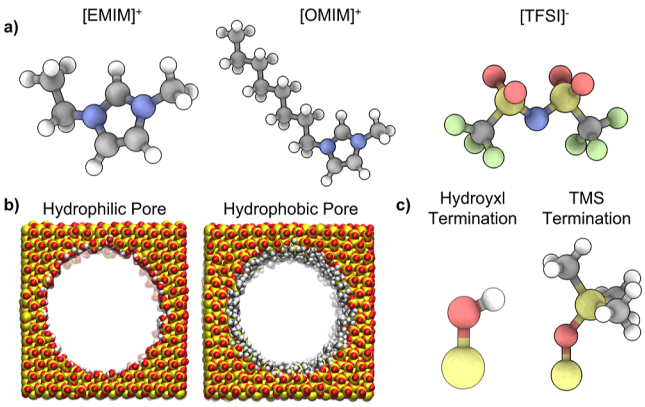

Figure 1. (a) Molecular structures of ILs $[EMIM]^+$, $[OMIM]^+$, and $[TFSI]^-$. (b) Molecular structure of the 5 nm diameter hydrophilic and hydrophobic pores. (c) Hydrogen (−H) that makes surface hydroxyls and trimethylsilyl (TMS, $-Si(CH_3)_3$) groups that terminate the hydrophilic and hydrophobic silica (SiO_2) pores, respectively. Gray = carbon, blue = nitrogen, red = oxygen, yellow = sulfur in $[TFSI]^-$, else silicon, green = fluorine, white = hydrogen.

CO_2 in the ILs does not follow the conventional Stokes−Einstein relation.[26] To expand on this work, here we used MD simulations to investigate CO_2 dissolved in aqueous and IL systems when confined in cylindrical, silica nanopores (3, 5, and 8 nm diameters) with hydrophilic and hydrophobic pore surface termination (Figure 1b,c). Moreover, we designed an interfacial system that transitions between hydrophobic and hydrophilic surface chemistry, allowing us to examine the IL/aqueous interface while under the effects of nanoconfinement. The more complex systems modeled here are designed to match the experimental conditions of the ultrathin enzymatic membrane better.

■ METHODS

Molecular Dynamics Parameters. Classical molecular dynamics (MD) simulations were performed using GROMACS (2021).[27,28] The leapfrog algorithm was used with a 1 fs time step. The velocity-rescaling thermostat with a coupling constant of 1 ps and a reference temperature of 298 K was used.[29] During the pore loading procedure (vide infra), the pressure was maintained using the Berendsen barostat and a 1 ps coupling constant.[30] The LINCS algorithm was used to constrain bond lengths for atoms bonded with hydrogen.[31] Short-range, nonbonded interactions were cutoff at 13 Å. The particle mesh Ewald (PME) method was used for long-range, nonbonded interactions.[32] Periodic boundary conditions were applied in all directions.

The ±0.8 charge IL force field parameters reported by Doherty et al. were used for $[EMIM]^+$, $[OMIM]^+$, and $[TFSI]^-$.[33] SPC/E parameters were used for water.[34] The parameters for CO_2 were taken from Cygan et al.[35] Parameters from Emami et al. were used for the silica pore[36] and the LigParGen web server was used to generate OPLS-AA compatible parameters for the trimethylsilyl (TMS) groups terminating the hydrophobic silica pore.[37]

Structure Generation. The PYTHON module PoreMS (0.2.0) was used to generate hydrophilic and hydrophobic silica pore initial structures of approximately 3, 5, and 8 nm pore diameter and a length of approximately 7 nm.[38] Hydrophilic pores were generated with 100% hydroxyl group coverage within the pore. Hydrophobic pores were generated by replacing 40% of the H in the hydroxyl groups with TMS groups. Due to the larger size of the TMS groups compared with the hydroxyl groups that were replaced, 40% coverage is near the maximum amount of TMS groups that can fit without collisions. While real silica surfaces typically have ∼9−18% hydroxyl group ionization at neutral pH, we did not include surface group ionization in our models. Previously, no major effects were observed by this degree of ionization (e.g., identical water density profiles in Emami et al. Figure 8).[36] The empty pore structures underwent an energy minimization with the steepest descent algorithm for 5000 steps, followed by a 500 ps NPT (i.e., constant temperature and pressure) simulation at 1 atm and 298 K. Afterward, the silica molecules were frozen in place for the remainder of the study; however, the hydroxyl and TMS functional groups attached to the silica pore interior remained mobile.

Bulk liquid IL/CO_2 simulation boxes were taken from our previous study[26] and are available on GitHub.[39] These simulation boxes contain 512 IL ion pairs and 100 CO_2 molecules. This mole fraction of CO_2 corresponds to that expected for [EMIM][TFSI] in equilibrium with a CO_2 partial pressure of ∼0.35 MPa.[40] This value is within the CO_2 partial pressures for either integrated gasification combined cycle (IGCC) synthesis gas after gasification or integrated reforming combined cycles (IRCC) synthesis gas after reforming.[41,42] The bulk H_2O/CO_2 simulation box was initially created in Packmol[43] with 149 CO_2 molecules and ∼10,000 H_2O molecules, chosen to match the CO_2 per nm_3 number density found in the IL systems. No N_2 was included in these systems as Fu et al. showed that an ultrathin enzymatic layer can serve as an N_2 barrier.[25]

Simulation Procedure. As the density of a liquid within nanoconfinement differs from that of the bulk liquid,[44,45] a pore loading procedure was developed instead of using the *gmx solvate* command. A simulation box was generated by placing an equilibrated bulk liquid box (i.e., IL/CO_2 or water/CO_2) next to the empty pore (Figure S1a). The system underwent an energy minimization, followed by an NPT simulation at elevated pressure to ensure rapid and complete loading of the liquid into the pore. The system then underwent an NPT simulation at 1 atm and 298 K (Figure S1b). This process of allowing the pore liquid to equilibrate with a liquid reservoir allows the liquid density within the pore to be dictated by the liquid−liquid and liquid−pore intermolecular interactions rather than simply constraining the pore liquid density to be the same as bulk liquid density. Finally, the reservoir liquid not located within the pore was removed, leaving only the pore as a periodic system (Figure S1c). The production runs were conducted in the NVT ensemble at 298 K for a minimum of 80 and 1000 ns for the water/CO_2 systems and IL/CO_2 systems, respectively. A similar procedure was used to generate interfacial pores with the IL and aqueous layers, which is described in detail in the Supporting Information.

Simulation Analysis. Radial distribution functions (RDFs), density profiles, spatial distribution functions, and continuous dimer existence autocorrelation functions (DACFs) were computed with TRAVIS.[46,47] Free energy surfaces were computed by the histogram reweighting methods using PLUMED.[48,49] The built-in GROMACS command *gmx msd* was used to calculate diffusion coefficients.[50] In the pore systems, the diffusion coefficient was computed only in the direction parallel to the pore walls. Molecular renderings in Figures 1a,c, 4, 6 and S6 were created using Speck[51] while the renderings in Figures 1b, 3, 7a, S1, S3−S5 were created using visual molecular dynamics (VMD).[52]

■ RESULTS AND DISCUSSION

Aqueous Pore Systems. We began by observing the hydrophilic pore systems containing only water and CO_2 molecules. In Figure 2, we show the diffusion coefficients and diffusion ratios, defined as the pore diffusion coefficient divided by the bulk diffusion coefficient, for water and CO_2 as a function of pore diameter. The diffusion coefficient was calculated using a linear regression fit of the mean-squared displacement (MSD) and the error bars are estimated by taking the difference of diffusion coefficients from fits over the two halves of the fit interval.[50] Here, we see that the diffusion coefficients of both water and CO_2 are reduced by confinement, yet the magnitude of this reduction is considerably greater for CO_2. The diffusion ratios obtained for confined

https://doi.org/10.1021/acs.langmuir.4c00542
Langmuir 2024, 40, 10615−10622

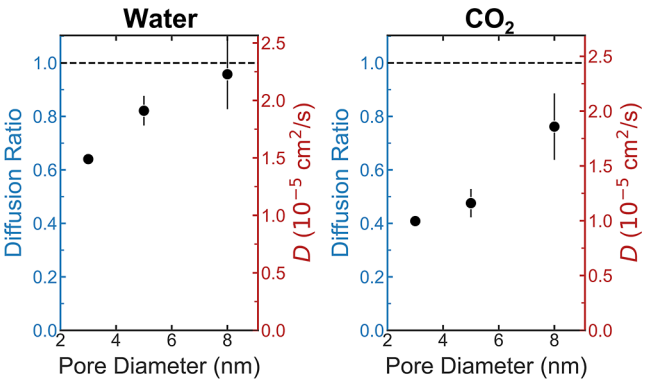

Figure 2. Diffusion coefficients of water (left) and CO_2 (right) in 3, 5, and 8 nm hydrophilic pores filled with water and CO_2. The left y-axis shows the diffusion coefficient compared against the value for an equivalent bulk solvent system while the right y-axis displays the diffusion coefficient absolute value. The dashed horizontal line denotes the bulk diffusion coefficient.

water are in excellent agreement with the experimental results. For example, Takahara et al. found the diffusion ratio of water confined in mesoporous silica (2.84 nm diameter) to be 0.63 using neutron scattering experiments[53] while the diffusion ratio we found for our 3 nm pore is 0.64 ± 0.02. In the largest hydrophilic pore, we find the absolute value of the CO_2 diffusion coefficient to be ~1.86 × 10^{-5} cm^2/s, which is more than 1 magnitude greater than the diffusion coefficient in an equivalently sized hydrophobic, IL-filled pore (vide infra).

To explain the difference in confinement effects on the transport of water and CO_2, we turn to the liquid structure. The number density of the CO_2 and H_2O molecules, starting at the center of the pore and proceeding radially, is shown in Figure 3 for the various pore diameters. For all pore sizes, the density of water molecules remains relatively constant within the pores. In contrast, the CO_2 density is greatly increased near the pore surface to values as high as 4 times the CO_2 density found near the center of the pore. This partitioning likely results from interactions between the surface hydroxyl group hydrogen bond donors and the CO_2 oxygens. Previously, researchers showed that CO_2/H_2O partitioning is much different near surfaces without hydroxyl groups (e.g., calcite[54]) where the surface can only act as a hydrogen bond acceptor, rather than a donor. The result of the partitioning seen here, with increased CO_2 near the pore walls, is that a much larger fraction of the CO_2 molecules interact with the mostly immobile pore surface groups. In fact, Figure 4 shows a two-dimensional combined radial/RDF, where the distances between each oxygen in CO_2 and different hydroxyl hydrogens on the pore surface are plotted. The most common orientation for CO_2 is where the molecule is aligned with the pore wall, and both oxygens are only 3.5 Å from hydroxyl hydrogens. These CO_2−OH interactions result in CO_2 having a smaller diffusion ratio compared with H_2O.

As the liquid structure dictates the diffusion ratio in these systems, we would expect that diffusion is a function of the CO_2 concentration. At larger concentrations of CO_2, we would expect more CO_2 near the center of the pore, as much of the pore wall is already occupied by CO_2 molecules. To test this hypothesis, we modeled two additional systems at ~3× and ~6× the concentration of CO_2. At triple the CO_2 concentration, the diffusion coefficient of CO_2 is modestly increased by ~8%, yet in the 6× system the diffusion

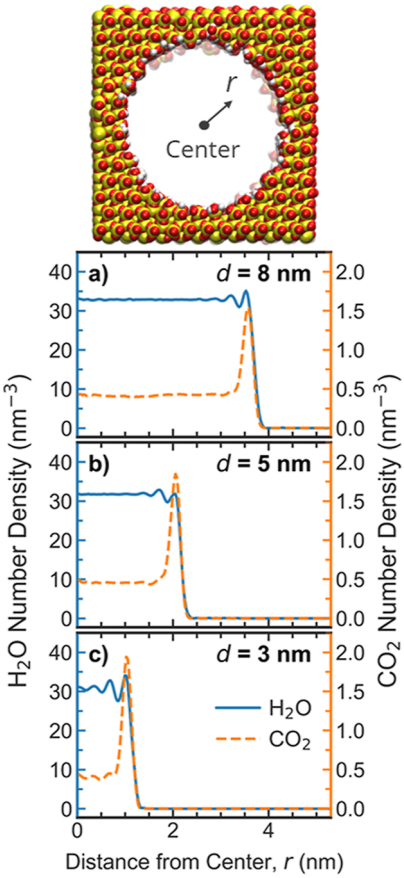

Figure 3. Number density of H_2O and CO_2 molecules shown as a function of distance from the center of the pore in the (a) 8, (b) 5, and (c) 3 nm hydrophilic pore systems filled with water and CO_2.

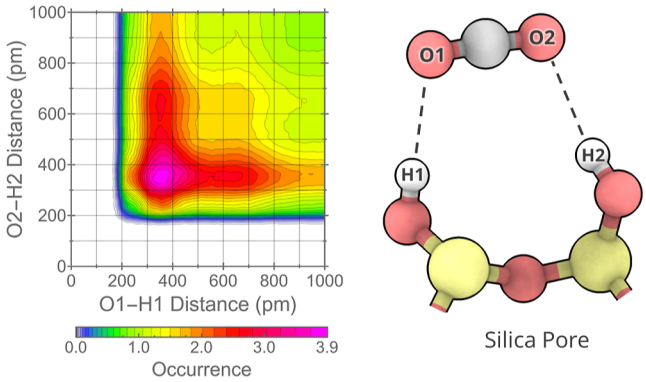

Figure 4. Combined radial/RDF for the two oxygen atoms in CO_2 and different hydroxyl group hydrogens on the pore surface illustrated by the schematic on the right. Gray = carbon, red = oxygen, yellow = silicon, white = hydrogen.

coefficient is dramatically reduced (Figure S2). Figure S3 shows snapshots comparing the initial system with the 6× CO_2 system, where it is clear that the CO_2 phase separates from the water in the high-concentration system but not in the initial system. In phase-separated systems, the boundary between CO_2 and H_2O serves as a barrier to diffusion, resulting in slow CO_2 diffusion along the length of the pore. Nevertheless, the typical CO_2 partial pressure in flue gas is not large enough to reach the CO_2 concentration modeled in this system (>0.14 CO_2 mole fraction). Within the expected concentration range

https://doi.org/10.1021/acs.langmuir.4c00542
Langmuir 2024, 40, 10615−10622

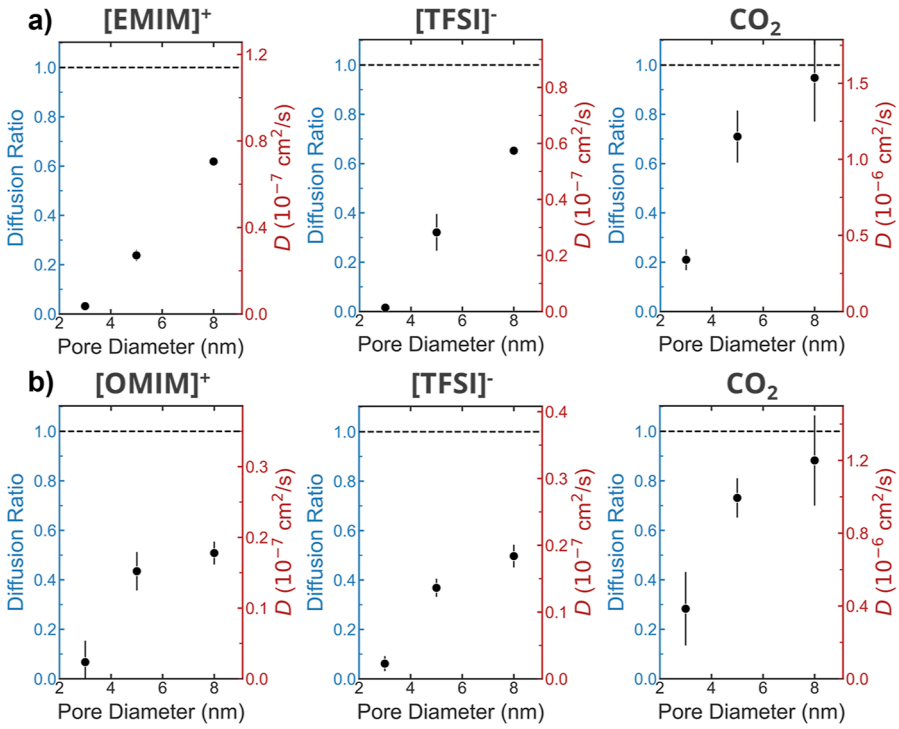

Figure 5. (a) Diffusion coefficients of $[EMIM]^+$ (left), $[TFSI]^-$ (middle), and CO_2 (right) as a function of hydrophobic pore size for the [EMIM][TFSI] system. (b) Diffusion coefficients of $[OMIM]^+$ (left), $[TFSI]^-$ (middle), and CO_2 (right) as a function of hydrophobic pore size for the [OMIM][TFSI] system. The left *y*-axis shows the diffusion coefficient compared against the value for an equivalent bulk liquid system while the right *y*-axis displays the diffusion coefficient absolute value. The dashed horizontal line denotes the bulk diffusion coefficient.

for CO_2, we expect greater concentrations of CO_2 to result in a small increase in the diffusion coefficient of CO_2 due to an increase in the level of CO_2 partitioning near the center of the pore.

$[EMIM]^+$ Pore Systems. Next, we observed the hydrophobic pore systems, constructed by replacing ∼40% of the pore hydrogens (−H) from the hydroxylated silica surfaces with trimethylsilyl groups (TMS, $-Si(CH_3)_3$), and loaded with either [EMIM][TFSI]/CO_2 or [OMIM][TFSI]/CO_2. The diffusion coefficients for $[EMIM]^+$, $[TFSI]^-$, and CO_2 as a function of the pore diameter in the [EMIM][TFSI]/CO_2 systems are shown in Figure 5a. The IL components show a significant decrease in diffusion coefficient, even in the largest diameter pore. At the smallest pore size, the $[EMIM]^+$ and $[TFSI]^-$ components are nearly frozen in place with diffusion ratios of only 0.031 and 0.015, respectively.

The diffusion coefficient of CO_2 in the 8 nm hydrophobic pore is not significantly different than that in bulk IL. This result contrasts with the equivalently sized aqueous pore system, where the diffusion coefficient of CO_2 is noticeably reduced relative to that within bulk water. One explanation for this difference is the reduction of surface hydroxyl (−OH) groups available to interact with the CO_2 molecules in the IL pore systems. While the hydrophobic pores still have some hydroxyl groups on the pore surface, these are obscured by the much larger TMS groups. This explanation is further supported by the density profiles of the $[EMIM]^+$, $[TFSI]^-$, and CO_2 within the hydrophobic pores, which show that the increase in CO_2 density near the pore surface is considerably smaller than the increase observed in the hydrophilic water/CO_2-filled pores (Figure S4). Nevertheless, in the smallest pore size, the CO_2 diffusion ratio drops to ∼0.21. This significant drop is likely due to interactions between the CO_2 and IL components, which are mostly immobile at this degree of confinement.

$[OMIM]^+$ Pore Systems. The diffusion coefficients for $[OMIM]^+$, $[TFSI]^-$, and CO_2 as a function of the pore diameter in the [OMIM][TFSI]/CO_2 system are shown in Figure 5b. In the 8 nm diameter pore, $[OMIM]^+$ and $[TFSI]^-$ undergo a larger reduction in diffusion coefficient compared with [EMIM][TFSI]. This reduction occurs because $[OMIM]^+$ is a larger molecule than $[EMIM]^+$ and, thus, the effects of confinement are comparatively greater. Counter-intuitively, we do not see the same trend in the 5 and 3 nm diameter pores. This result arises because of important properties of ILs that make them unique and useful materials—their irregular and asymmetrical shapes. In bulk liquid, the asymmetrical shape of ILs prevents efficient packing and results in ILs remaining liquid at room temperature despite strong intermolecular forces. Under nanoconfinement in the 3 nm pores, we see a similar effect where $[OMIM]^+$, having a much larger alkyl group and more asymmetric shape than $[EMIM]^+$, cannot undergo efficient packing, maintains a larger diffusion ratio, and more liquid character when compared with $[EMIM]^+$. This explanation can be corroborated by comparing the density profile for the [OMIM][TFSI]/CO_2 system (Figure S5c) to that of the [EMIM][TFSI]/CO_2 system (Figure S4c). Here, the density profiles can be interpreted similarly to RDFs, where particularly large peak values along with small valley values indicate highly structured or immobilized fluids.[55] When looking at the prominent features in the density profiles, the maximum and minimum closest to the pore wall, we find a higher degree of structure for the $[EMIM]^+$ system, with an average maximum value/minimum value ratio of 6.45 for the three liquid components, compared with the $[OMIM]^+$ system ratio of only 3.78. This result

https://doi.org/10.1021/acs.langmuir.4c00542
Langmuir 2024, 40, 10615−10622

confirms that the long $[OMIM]^+$ alkyl tail disrupts the packing of all liquid components and results in larger diffusion ratios in the 3 nm pore when compared with the $[EMIM]^+$ counterpart system.

The diffusion coefficient of CO_2 in the [OMIM][TFSI]/CO_2 system is similar to those of the IL components. At the largest pore size, the diffusion ratio for CO_2 in the $[OMIM]^+$ system is smaller than that for CO_2 in the $[EMIM]^+$ system, yet this trend is once again broken at the smaller pore diameters. Interestingly, in the 3 nm pore system, the absolute diffusion coefficient of CO_2 is larger in the $[OMIM]^+$ system compared to that in the $[EMIM]^+$ system (albeit within the error of the MD simulations). This finding is surprising as bulk [OMIM][TFSI] is ∼3× more viscous than bulk [EMIM]-[TFSI][56] and we had previously found that CO_2 diffuses faster in bulk [EMIM][TFSI] relative to bulk [OMIM][TFSI];[26] however, the nanoconfinement effects of the 3 nm pore disrupt the liquid structure of [OMIM][TFSI]/CO_2 comparatively more than [EMIM][TFSI]/CO_2, enough to reverse this trend. Moreover, CO_2-$[EMIM]^+$ and CO_2-$[OMIM]^+$ RDFs for bulk liquid and all three pore sizes are shown in Figure S6, allowing us to see the effect of pore size on the CO_2/cation structure directly. For both ILs, the RDFs for the bulk, 8 nm pore, and 5 nm pore systems are similar. Nevertheless, for the 3 nm pore systems, we observe an increase in the first maximum value for some of the CO_2-$[EMIM]^+$ RDFs, while we observe a decrease in the first maximum values for all of the CO_2-$[OMIM]^+$ RDFs. These data indicate that, in the 3 nm pores, the $[EMIM]^+$ system is more structured than the $[OMIM]^+$ system, consistent with the density profiles and the diffusion coefficients.

CO_2/Cation Interactions. The RDFs shown here and those reported in the literature show strong associations between various imidazolium cation atoms and CO_2 atoms.[26,57] This observation poses a question as to how, under nanoconfinement, the CO_2 diffusion ratio is larger than that of the imidazolium cations with which they appear to be strongly interacting with. To elucidate this result, we examined the continuous dimer existence autocorrelation functions (DACFs) for the methyl carbon on the imidazolium cation and carbon in CO_2 shown in Figure 6. The methyl carbon on the cation was chosen for this analysis as it shows the strongest interaction with CO_2 and a dimer cutoff value of 5.2 Å was chosen based on the distance where the first solvation shell ends in the RDFs (Figure S6). Here, we see that nanoconfinement destabilizes the CO_2 solvation of the imidazolium cations, resulting in shorter dimer lifetimes. Nevertheless, the RDFs in Figure S6 for the bulk, 8, and 5 nm systems show little differences under confinement. Therefore, under confinement, the amount of time a CO_2 molecule interacts with an individual imidazolium cation decreases, but the likelihood that a CO_2 is interacting with *any* imidazolium cation is comparable to that in the bulk. As such, the diffusion ratio of CO_2 exceeds that of the imidazolium cation component because the CO_2 molecules are jumping between imidazolium cations more frequently.

Interfacial Aqueous/IL Systems. Finally, we constructed interfacial systems with a pore diameter of 5 nm which contain regions of hydrophilic and hydrophobic surface groups with water/CO_2 loaded into the hydrophilic region and IL/CO_2 loaded into the hydrophobic region. A snapshot of the [EMIM][TFSI]/CO_2/H_2O system is shown in Figure 7a and the schematic for a CO_2 capture device with aqueous and IL layers, that incorporates an enzymatic capture layer, is shown in Figure 7b. Free energy profiles for the CO_2 and H_2O components in the $[EMIM]^+$ and $[OMIM]^+$ systems are shown in Figure 8a,b, respectively. In both systems, CO_2 has a negative free energy (ΔG) in the IL phase, indicating favorable transport from the water to the IL phase. The magnitude of ΔG is comparable for $[EMIM]^+$ ($\Delta G \sim -4.62$ kJ/mol) and $[OMIM]^+$ ($\Delta G \sim -3.97$ kJ/mol) solutions. These values are slightly less than the values found in bulk (−5.86 and −5.66 kJ/mol for the $[EMIM]^+$ and $[OMIM]^+$ systems).[26] This reduction could be a result of the hydroxyl groups in the hydrophilic region making the water phase more favorable and, by comparison, reducing the ΔG when transported from the aqueous to IL phases. Conversely, the ΔG for H_2O is positive and large (14.39 and 17.28 kJ/mol for the $[EMIM]^+$ and $[OMIM]^+$ systems), indicating that H_2O molecules prefer maintaining a separate phase and do not mix with the IL components.

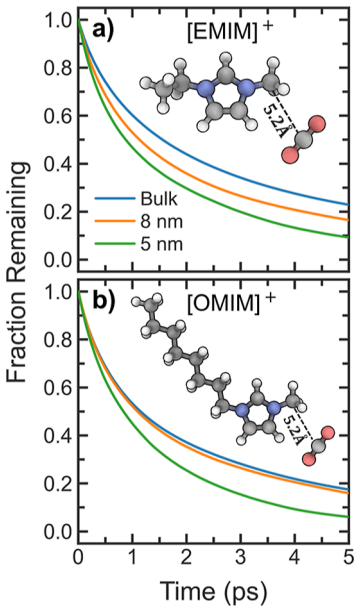

Figure 6. Dimer existence autocorrelation functions for (a) $[EMIM]^+$-CO_2 and (b) $[OMIM]^+$-CO_2 dimer pairs in bulk and 8 and 5 nm pores.

■ CONCLUSIONS

CO_2 separation membranes are a critical technology to reduce emissions. Our MD results reveal numerous insights that can help us understand and improve CO_2 separation membrane technologies. In confined aqueous systems, a large density of hydroxyl groups results in increased CO_2 density near the pore walls and an overall greater reduction in diffusion in the axial direction of the pore, even at the relatively large pore diameter of 8 nm. Conversely, in [EMIM][TFSI] and [OMIM][TFSI], CO_2 maintains diffusion rates comparable to those of the bulk in 8 nm hydrophobic pores. Counterintuitively, at greater degrees of nanoconfinement (e.g., 3 nm diameter), bulkier and more asymmetric ILs (e.g., $[OMIM]^+$ as opposed to $[EMIM]^+$) may undergo less efficient packing, allowing the system to maintain a higher liquid character and faster diffusion rates. We expect this phenomenon, where asymmetric ILs maintain more liquid character under confinement, to be generalizable to other nanoconfined IL membrane systems. The nanoconfined [EMIM][TFSI]/H_2O and [OMIM]-

https://doi.org/10.1021/acs.langmuir.4c00542
Langmuir 2024, 40, 10615−10622

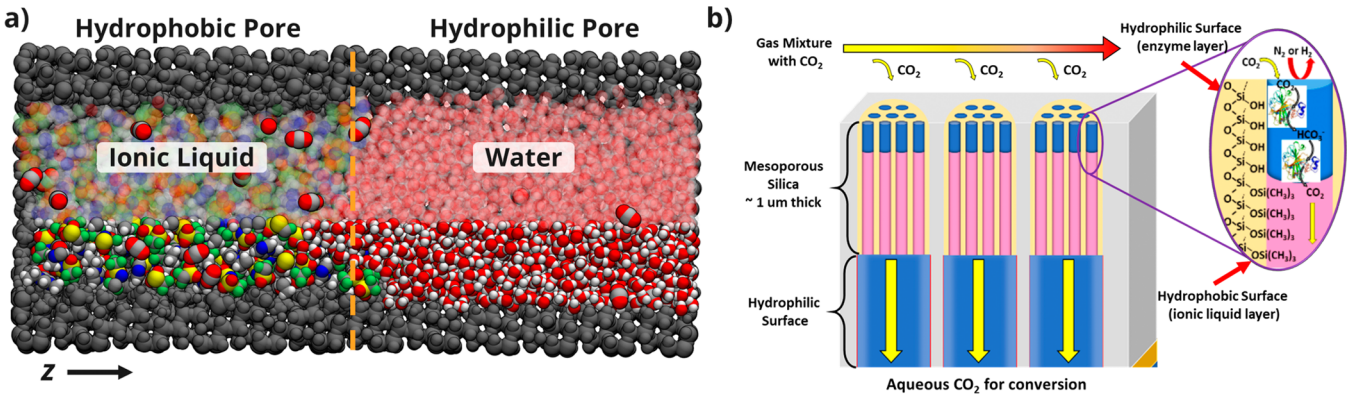

Figure 7. (a) Snapshot of [EMIM][TFSI]/H_2O sliced open with the hydrophobic and hydrophilic surface termination to the left and right of the dashed orange line, respectively. CO_2 emphasized to show presence located predominately in the IL phase. Gray = carbon, blue = nitrogen, red = oxygen, yellow = sulfur, green = fluorine, white = hydrogen, dark gray = pore. (b) Schematic of nanoporous CO_2 capture device with aqueous layers (blue) and IL layer (pink).

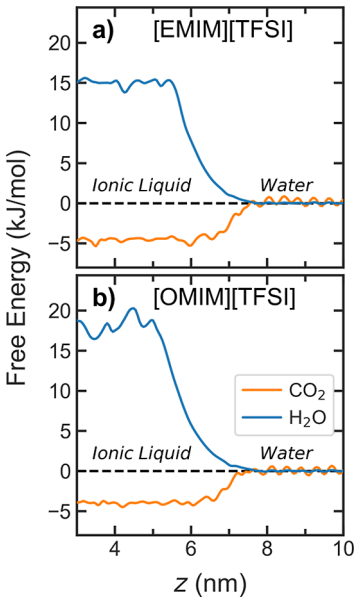

Figure 8. Free energy profiles for CO_2 and H_2O in the (a) [EMIM][TFSI]/H_2O and (b) [OMIM][TFSI]/H_2O interfacial, 5 nm diameter pores. The interface between the IL and water occurs at $z \sim 7$ nm.

[TFSI]/H_2O systems modeled here maintain separate IL and aqueous phases, where CO_2 is shown to transport spontaneously from the aqueous to the IL phase. Future experimental studies, such as with pulsed-field gradient nuclear magnetic resonance spectroscopy and neutron scattering, could look to verify the structure and diffusion rates of nanoconfined imidazolium ILs and CO_2.

■ ASSOCIATED CONTENT

Supporting Information

The Supporting Information is available free of charge at https://pubs.acs.org/doi/10.1021/acs.langmuir.4c00542.

Supporting Figures S1−S6 showing IL and carbon dioxide density profiles, cation/carbon dioxide RDFs, a schematic illustration of the pore loading procedure, snapshots from aqueous systems with an increased concentration of CO_2, and diffusion coefficients for aqueous systems with an increased concentration of CO_2 (PDF)

■ AUTHOR INFORMATION

Corresponding Authors

Juan M. Vanegas − *Department of Biochemistry and Biophysics, Oregon State University, Corvallis, Oregon 97331, United States;* orcid.org/0000-0003-1381-1649; Email: vanegasj@oregonstate.edu

Susan B. Rempe − *Center for Integrated Nanotechnologies, Sandia National Laboratories, Albuquerque, New Mexico 87185, United States;* orcid.org/0000-0003-1623-2108; Email: slrempe@sandia.gov

Authors

Calen J. Leverant − *Nanoscale Sciences Department, Sandia National Laboratories, Albuquerque, New Mexico 87185, United States;* orcid.org/0000-0003-1343-2841

Danielle Richards − *Electronic, Optical, and Nano Department, Sandia National Laboratories, Albuquerque, New Mexico 87185, United States*

Erik D. Spoerke − *Electronic, Optical, and Nano Department, Sandia National Laboratories, Albuquerque, New Mexico 87185, United States;* orcid.org/0000-0003-2286-2560

Ryan Alcala − *MemZyme, LLC, Albuquerque, New Mexico 87123, United States*

Ying-Bing Jiang − *MemZyme, LLC, Albuquerque, New Mexico 87123, United States*

Stephen J. Percival − *Electronic, Optical, and Nano Department, Sandia National Laboratories, Albuquerque, New Mexico 87185, United States;* orcid.org/0000-0003-2067-7468

Complete contact information is available at: https://pubs.acs.org/10.1021/acs.langmuir.4c00542

Notes

The authors declare no competing financial interest.

■ ACKNOWLEDGMENTS

This work was performed, in part, at the Center for Integrated Nanotechnologies, an Office of Science User Facility operated for the U.S. Department of Energy (DOE) Office of Science. This work was fully supported by the Laboratory Directed Research and Development (LDRD) program of Sandia

National Laboratories. Sandia National Laboratories is a multimission laboratory managed and operated by National Technology & Engineering Solutions of Sandia, LLC, a wholly owned subsidiary of Honeywell International Inc., for the U.S. Department of Energy's National Nuclear Security Administration under contract DE-NA0003525. This paper describes objective technical results and analysis. Any subjective views or opinions that might be expressed in the paper do not necessarily represent the views of the U.S. Department of Energy of the United States Government. This article has been authored by an employee of National Technology & Engineering Solutions of Sandia, LLC under Contract No. DE-NA0003525 with the U.S. Department of Energy (DOE). The employee owns all rights, titles, and interests in and to the article and is solely responsible for its contents. The United States Government retains and the publisher, by accepting the article for publication, acknowledges that the United States Government retains a nonexclusive, paid-up, irrevocable, worldwide license to publish or reproduce the published form of this article or allow others to do so, for United States Government purposes. The DOE will provide public access to these results of federally sponsored research in accordance with the DOE Public Access Plan https://www.energy.gov/downloads/doe-public-access-plan.

■ REFERENCES

(1) Austen Angell, C.; Ansari, Y.; Zhao, Z. Ionic Liquids: Past, present and future. *Faraday Discuss.* **2012**, *154*, 9−27.

(2) Lei, Z.; Chen, B.; Koo, Y.-M.; MacFarlane, D. R. Introduction: Ionic Liquids. *Chem. Rev.* **2017**, *117*, 6633−6635.

(3) Ludwig, R.; Kragl, U. Do We Understand the Volatility of Ionic Liquids? *Angew. Chem., Int. Ed.* **2007**, *46*, 6582−6584.

(4) Blanchard, L. A.; Hancu, D.; Beckman, E. J.; Brennecke, J. F. Green processing using ionic liquids and CO_2. *Nature* **1999**, *399*, 28−29.

(5) Seddon, K. R. Ionic Liquids for Clean Technology. *J. Chem. Technol. Biotechnol.* **1997**, *68*, 351−356.

(6) Boot-Handford, M. E.; Abanades, J. C.; Anthony, E. J.; Blunt, M. J.; Brandani, S.; Mac Dowell, N.; Fernández, J. R.; Ferrari, M. C.; Gross, R.; Hallett, J. P.; et al. Carbon capture and storage update. *Energy Environ. Sci.* **2014**, *7*, 130−189.

(7) Ramdin, M.; de Loos, T. W.; Vlugt, T. J. State-of-the-Art of CO_2 Capture with Ionic Liquids. *Ind. Eng. Chem. Res.* **2012**, *51*, 8149−8177.

(8) Luo, X.; Guo, Y.; Ding, F.; Zhao, H.; Cui, G.; Li, H.; Wang, C. Significant Improvements in CO_2 Capture by Pyridine-Containing Anion-Functionalized Ionic Liquids through Multiple-Site Cooperative Interactions. *Angew. Chem., Int. Ed.* **2014**, *53*, 7053−7057.

(9) Revelli, A.-L.; Mutelet, F.; Jaubert, J.-N. High Carbon Dioxide Solubilities in Imidazolium-Based Ionic Liquids and in Poly(ethylene glycol) Dimethyl Ether. *J. Phys. Chem. B* **2010**, *114*, 12908−12913.

(10) Zeng, S.; Wang, J.; Bai, L.; Wang, B.; Gao, H.; Shang, D.; Zhang, X.; Zhang, S. Highly Selective Capture of CO_2 by Ether-Functionalized Pyridinium Ionic Liquids with Low Viscosity. *Energy Fuels* **2015**, *29*, 6039−6048.

(11) Palomar, J.; Gonzalez-Miquel, M.; Polo, A.; Rodriguez, F. Understanding the Physical Absorption of CO_2 in Ionic Liquids Using the COSMO-RS Method. *Ind. Eng. Chem. Res.* **2011**, *50*, 3452−3463.

(12) Moya, C.; Palomar, J.; Gonzalez-Miquel, M.; Bedia, J.; Rodriguez, F. Diffusion Coefficients of CO_2 in Ionic Liquids Estimated by Gravimetry. *Ind. Eng. Chem. Res.* **2014**, *53*, 13782−13789.

(13) Gonzalez-Miquel, M.; Bedia, J.; Palomar, J.; Rodriguez, F. Solubility and Diffusivity of CO2 in [hxmim] [NTf2], [omim] [NTf2], and [dcmim] [NTf2] at T = (298.15, 308.15, and 323.15) K and Pressures up to 20 bar. *J. Chem. Eng. Data* **2014**, *59*, 212−217.

(14) de Riva, J.; Suarez-Reyes, J.; Moreno, D.; Díaz, I.; Ferro, V.; Palomar, J. Ionic liquids for post-combustion CO2 capture by physical absorption: Thermodynamic, kinetic and process analysis. *Int. J. Greenhouse Gas Control* **2017**, *61*, 61−70.

(15) Hospital-Benito, D.; Lemus, J.; Moya, C.; Santiago, R.; Ferro, V.; Palomar, J. Techno-economic feasibility of ionic liquids-based CO2 chemical capture processes. *Chem. Eng. J.* **2021**, *407*, 127196.

(16) Liu, Y.; Yang, Y.; Qu, Y.; Li, Y.-Q.; Zhao, M.; Li, W. Interface-enhanced CO2 capture via the synthetic effects of a nanomaterial-supported ionic liquid thin film. *Nanoscale Adv.* **2021**, *3*, 1397−1403.

(17) Wang, S.; Li, X.; Wu, H.; Tian, Z.; Xin, Q.; He, G.; Peng, D.; Chen, S.; Yin, Y.; Jiang, Z.; et al. Advances in high permeability polymer-based membrane materials for CO_2 separations. *Energy Environ. Sci.* **2016**, *9*, 1863−1890.

(18) Bara, J. E.; Camper, D. E.; Gin, D. L.; Noble, R. D. Room-Temperature Ionic Liquids and Composite Materials: Platform Technologies for CO_2 Capture. *Acc. Chem. Res.* **2010**, *43*, 152−159.

(19) Bara, J. E.; Gabriel, C. J.; Carlisle, T. K.; Camper, D. E.; Finotello, A.; Gin, D. L.; Noble, R. D. Gas separations in fluoroalkyl-functionalized room-temperature ionic liquids using supported liquid membranes. *Chem. Eng. J.* **2009**, *147*, 43−50.

(20) Hojniak, S. D.; Silverwood, I. P.; Khan, A. L.; Vankelecom, I. F. J.; Dehaen, W.; Kazarian, S. G.; Binnemans, K. Highly Selective Separation of Carbon Dioxide from Nitrogen and Methane by Nitrile/Glycol-Difunctionalized Ionic Liquids in Supported Ionic Liquid Membranes (SILMs). *J. Phys. Chem. B* **2014**, *118*, 7440−7449.

(21) Lozano, L.; Godínez, C.; de los Ríos, A.; Hernández-Fernández, F.; Sánchez-Segado, S.; Alguacil, F. Recent advances in supported ionic liquid membrane technology. *J. Membr. Sci.* **2011**, *376*, 1−14.

(22) Scovazzo, P.; Kieft, J.; Finan, D. A.; Koval, C.; DuBois, D.; Noble, R. Gas separations using non-hexafluorophosphate [PF6]-anion supported ionic liquid membranes. *J. Membr. Sci.* **2004**, *238*, 57−63.

(23) Budhathoki, S.; Shah, J. K.; Maginn, E. J. Molecular Simulation Study of the Performance of Supported Ionic Liquid Phase Materials for the Separation of Carbon Dioxide from Methane and Hydrogen. *Ind. Eng. Chem. Res.* **2017**, *56*, 6775−6784.

(24) Park, H. B.; Kamcev, J.; Robeson, L. M.; Elimelech, M.; Freeman, B. D. Maximizing the right stuff: The trade-off between membrane permeability and selectivity. *Science* **2017**, *356*, No. eaab0530.

(25) Fu, Y.; Jiang, Y.-B.; Dunphy, D.; Xiong, H.; Coker, E.; Chou, S. S.; Zhang, H.; Vanegas, J. M.; Croissant, J. G.; Cecchi, J. L.; et al. Ultra-thin enzymatic liquid membrane for CO_2 separation and capture. *Nat. Commun.* **2018**, *9*, 990.

(26) Sharma, A.; Leverant, C. J.; Richards, D.; Beamis, C. P.; Spoerke, E. D.; Percival, S. J.; Rempe, S. B.; Vanegas, J. M. Transport and Energetics of Carbon Dioxide in Ionic Liquids at Aqueous Interfaces. *J. Phys. Chem. B* **2023**, *127*, 10573−10582.

(27) Abraham, M. J.; Murtola, T.; Schulz, R.; Páll, S.; Smith, J. C.; Hess, B.; Lindahl, E. GROMACS: High performance molecular simulations through multi-level parallelism from laptops to supercomputers. *SoftwareX* **2015**, *1−2*, 19−25.

(28) Van Der Spoel, D.; Lindahl, E.; Hess, B.; Groenhof, G.; Mark, A. E.; Berendsen, H. J. C. GROMACS: Fast, flexible, and free. *J. Comput. Chem.* **2005**, *26*, 1701−1718.

(29) Bussi, G.; Donadio, D.; Parrinello, M. Canonical sampling through velocity rescaling. *J. Chem. Phys.* **2007**, *126*, 014101.

(30) Berendsen, H. J. C.; Postma, J. P. M.; van Gunsteren, W. F.; DiNola, A.; Haak, J. R. Molecular dynamics with coupling to an external bath. *J. Chem. Phys.* **1984**, *81*, 3684−3690.

(31) Hess, B.; Bekker, H.; Berendsen, H. J. C.; Fraaije, J. G. E. M. LINCS: A linear constraint solver for molecular simulations. *J. Comput. Chem.* **1997**, *18*, 1463−1472.

(32) Darden, T.; York, D.; Pedersen, L. Particle mesh Ewald: An $N\cdot\log(N)$ method for Ewald sums in large systems. *J. Chem. Phys.* **1993**, *98*, 10089−10092.

(33) Doherty, B.; Zhong, X.; Gathiaka, S.; Li, B.; Acevedo, O. Revisiting OPLS Force Field Parameters for Ionic Liquid Simulations. *J. Chem. Theory Comput.* **2017**, *13*, 6131−6145.
(34) Berendsen, H. J. C.; Grigera, J. R.; Straatsma, T. P. The missing term in effective pair potentials. *J. Phys. Chem.* **1987**, *91*, 6269−6271.
(35) Cygan, R. T.; Romanov, V. N.; Myshakin, E. M. Molecular Simulation of Carbon Dioxide Capture by Montmorillonite Using an Accurate and Flexible Force Field. *J. Phys. Chem. C* **2012**, *116*, 13079−13091.
(36) Emami, F. S.; Puddu, V.; Berry, R. J.; Varshney, V.; Patwardhan, S. V.; Perry, C. C.; Heinz, H. Force Field and a Surface Model Database for Silica to Simulate Interfacial Properties in Atomic Resolution. *Chem. Mater.* **2014**, *26*, 2647−2658.
(37) Dodda, L. S.; Cabeza de Vaca, I.; Tirado-Rives, J.; Jorgensen, W. L. LigParGen web server: an automatic OPLS-AA parameter generator for organic ligands. *Nucleic Acids Res.* **2017**, *45*, W331−W336.
(38) Kraus, H.; Rybka, J.; Höltzel, A.; Trebel, N.; Tallarek, U.; Hansen, N. PoreMS: a software tool for generating silica pore models with user-defined surface functionalisation and pore dimensions. *Mol. Simul.* **2021**, *47*, 306−316.
(39) Sharma-JPCB-ionic-liquids-CO2. 2023 https://github.com/vanegasj/Sharma-JPCB-ionic-liquids-CO2 (accessed February 14, 2024).
(40) Makino, T.; Kanakubo, M.; Masuda, Y.; Umecky, T.; Suzuki, A. CO2 absorption properties, densities, viscosities, and electrical conductivities of ethylimidazolium and 1-ethyl-3-methylimidazolium ionic liquids. *Fluid Phase Equilib.* **2014**, *362*, 300−306.
(41) Metz, B.; Davidson, O.; Coninck, H. d.; Loos, M.; Meyer, L. *IPCC Special Report on Carbon Dioxide Capture and Storage*, 2005.
(42) Kothandaraman, A.; Nord, L.; Bolland, O.; Herzog, H. J.; McRae, G. J. Comparison of solvents for post-combustion capture of CO2 by chemical absorption. *Energy Procedia* **2009**, *1*, 1373−1380.
(43) Martínez, L.; Andrade, R.; Birgin, E. G.; Martínez, J. M. PACKMOL: A package for building initial configurations for molecular dynamics simulations. *J. Comput. Chem.* **2009**, *30*, 2157−2164.
(44) Lerbret, A.; Lelong, G.; Mason, P. E.; Saboungi, M. L.; Brady, J. W. Water Confined in Cylindrical Pores: A Molecular Dynamics Study. *Food Biophys.* **2011**, *6*, 233−240.
(45) Zaragoza, A.; Gonzalez, M. A.; Joly, L.; López-Montero, I.; Canales, M. A.; Benavides, A. L.; Valeriani, C. Molecular dynamics study of nanoconfined TIP4P/2005 water: how confinement and temperature affect diffusion and viscosity. *Phys. Chem. Chem. Phys.* **2019**, *21*, 13653−13667.
(46) Brehm, M.; Kirchner, B. TRAVIS - A Free Analyzer and Visualizer for Monte Carlo and Molecular Dynamics Trajectories. *J. Chem. Inf. Model.* **2011**, *51*, 2007−2023.
(47) Brehm, M.; Thomas, M.; Gehrke, S.; Kirchner, B. TRAVIS—A free analyzer for trajectories from molecular simulation. *J. Chem. Phys.* **2020**, *152*, 164105.
(48) Bonomi, M.; Branduardi, D.; Bussi, G.; Camilloni, C.; Provasi, D.; Raiteri, P.; Donadio, D.; Marinelli, F.; Pietrucci, F.; Broglia, R. A.; et al. PLUMED: A portable plugin for free-energy calculations with molecular dynamics. *Comput. Phys. Commun.* **2009**, *180*, 1961−1972.
(49) Tribello, G. A.; Bonomi, M.; Branduardi, D.; Camilloni, C.; Bussi, G. PLUMED 2: New feathers for an old bird. *Comput. Phys. Commun.* **2014**, *185*, 604−613.
(50) Abraham, M.; et al. *GROMACS 2023.3 Manual*, 2023.
(51) *Speck: Browser-based webgl Molecule renderer with the goal of producing figures that are as attractive as they are practical.* 2022 https://github.com/wwwtyro/speck.
(52) Humphrey, W.; Dalke, A.; Schulten, K. VMD − Visual Molecular Dynamics. *J. Mol. Graph.* **1996**, *14*, 33−38.
(53) Takahara, S.; Sumiyama, N.; Kittaka, S.; Yamaguchi, T.; Bellissent-Funel, M.-C. Neutron Scattering Study on Dynamics of Water Molecules in MCM-41. 2. Determination of Translational Diffusion Coefficient. *J. Phys. Chem. B* **2005**, *109*, 11231−11239.
(54) Ali, A.; Striolo, A.; Cole, D. R. CO2 Solubility in Aqueous Electrolyte Solutions Confined in Calcite Nanopores. *J. Phys. Chem. C* **2021**, *125*, 12333−12341.
(55) Leverant, C. J.; Greathouse, J. A.; Harvey, J. A.; Alam, T. M. Machine Learning Predictions of Simulated Self-Diffusion Coefficients for Bulk and Confined Pure Liquids. *J. Chem. Theory Comput.* **2023**, *19*, 3054−3062.
(56) Tariq, M.; Carvalho, P. J.; Coutinho, J. A.; Marrucho, I. M.; Lopes, J. N. C.; Rebelo, L. P. N. Viscosity of (C2−C14) 1-alkyl-3-methylimidazolium bis (trifluoromethylsulfonyl) amide ionic liquids in an extended temperature range. *Fluid Phase Equilib.* **2011**, *301*, 22−32.
(57) Jung, A.; Řeha, D.; Minofar, B.; Stanovský, P.; Pasichnyk, M.; Přibyl, M.; Bara, J. E.; Friess, K.; Fíla, V.; Izák, P. Molecular simulation of poly(VDF-HFP) copolymer with imidazolium-based ionic liquid as an effective medium for biogas separation. *J. Mol. Liq.* **2022**, *366*, 120287.

https://doi.org/10.1021/acs.langmuir.4c00542
Langmuir 2024, 40, 10615−10622